


Article

Chemical Speciation of Antarctic Atmospheric Depositions

Stefano Bertinetti ¹, Silvia Berto ^{1,*}, Mery Malandrino ¹, Davide Vione ¹, Ornella Abollino ²,
Eleonora Conca ¹, Matteo Marafante ¹, Anna Annibaldi ³, Cristina Truzzi ³ and Silvia Illuminati ³

¹ Department of Chemistry, Università di Torino, Via P. Giuria 7, 10125 Turin, Italy; stefano.bertinetti@unito.it (S.B.); mery.malandrino@unito.it (M.M.); davide.vione@unito.it (D.V.); eleonora.conca@unito.it (E.C.); matteo.marafante@edu.unito.it (M.M.)

² Department of Drug Science and Technology, Università di Torino, Via P. Giuria 9, 10125 Turin, Italy; ornella.abollino@unito.it

³ Department of Life and Environmental Sciences, Università Politecnica delle Marche, Via Brecce Bianche, 60131 Ancona, Italy; a.annibaldi@univpm.it (A.A.); c.truzzi@univpm.it (C.T.); s.illuminati@staff.univpm.it (S.I.)

* Correspondence: silvia.berto@unito.it; Tel.: +39-0116705279

Featured Application: The results of such studies will enable researchers to gain insight into the behavior of metals in wet depositions, which is fundamental knowledge to carry out atmospheric photochemistry studies and to model biogeochemical cycles of metal cations.

Abstract: Both inorganic and organic complexation of metal cations in clouds or rainwater is essential to describe the global biogeochemical cycles of metals, because complexation can increase metal solubility and stabilize some of their oxidation states. Within a Project of the National Research Program in the Antarctica, atmospheric depositions were collected during the Antarctic summer 2017–2018 in eight sampling sites. The main ionic components occurring in water extracts of these atmospheric depositions were quantified, and a chemical model was applied, in order to identify the main species occurring in the samples. The speciation study showed that most cations were present as aquoions, except for Fe, which occurred predominantly in hydrolytic forms. The model allowed us to foresee the effect of an increase in the concentration levels of all the solution components, by simulating what could happen when the original particles act as cloud condensation nuclei. The role of inorganic anions as complexing agents becomes important when increasing total concentrations of all the solutes by a factor >100 compared to the water extracts, while the presence of organic acids acquires significance for samples having organic acid concentration higher than 10^{-5} mol L⁻¹. Moreover, it was possible to pinpoint the formation constants that mostly affect the chemical system, and to gain insight into the behavior of metals in wet depositions, which is fundamental knowledge in atmospheric photochemistry studies and in the modeling of the biogeochemical cycles of metal cations.

Keywords: Antarctica; atmospheric depositions; metal complexes; metal speciation; chemical modeling; metal cations



Citation: Bertinetti, S.; Berto, S.; Malandrino, M.; Vione, D.; Abollino, O.; Conca, E.; Marafante, M.; Annibaldi, A.; Truzzi, C.; Illuminati, S. Chemical Speciation of Antarctic Atmospheric Depositions. *Appl. Sci.* **2022**, *12*, 4438. <https://doi.org/10.3390/app12094438>

Academic Editors: Franz Saija, Ottavia Giuffrè, Giuseppe Cassone and Claudia Foti

Received: 5 April 2022

Accepted: 22 April 2022

Published: 27 April 2022

Publisher's Note: MDPI stays neutral with regard to jurisdictional claims in published maps and institutional affiliations.



Copyright: © 2022 by the authors. Licensee MDPI, Basel, Switzerland. This article is an open access article distributed under the terms and conditions of the Creative Commons Attribution (CC BY) license (<https://creativecommons.org/licenses/by/4.0/>).

1. Introduction

The atmosphere plays an important role in the geochemical cycles of the metal cations. For instance, the atmospheric deposition of mineral dust from continental regions is a known and significant source of both iron and aluminum to the open ocean [1,2]. When studying iron atmospheric deposition in the eastern Atlantic Ocean, Sarthou et al. [3] found that wet deposition dominates in the intertropical convergence zone. In contrast, dry deposition dominates in the other regions. Jickells et al. [1] reported that 30 to 95% of total dust removal occurs by wet deposition.

Moreover, Fe plays a fundamental role in the control of biomass production in the oceans, especially for those waters that are labeled as High Nutrient Low Chlorophyll

(HNLC), such as the Southern Ocean (SO) [4]. Mineral dust has been recognized to play a secondary role as a source of Fe and other metallic elements for the surface ecosystems of SO, when compared to inputs from sediments and the upwelling of nutrient-rich waters [5,6]. However, the strong correlation between atmospheric mineral dust fluxes and climate conditions makes mineral dust a notable Fe source, especially for those regions that, like the SO, are quite susceptible to variations in the input magnitude [7]. The release of soluble species from mineral dust to ocean water can happen directly following atmospheric deposition, or occur after melting of snow and ice, on which the atmospheric particulate has previously accumulated. Part of the dust can be dissolved in atmospheric droplets or melting water, and thus the chemical processes that occur in the soluble fraction of the aerosol may affect the speciation, the photo-reactivity, and the bioavailability of metal cations [8–10]. The percentage of water-soluble Fe and Al in the Antarctic aerosol is quite low, and has been shown to vary from 10% to 20% with respect to the total concentrations [11]. However, inorganic and organic complexation can enhance the solubility of metal cations and stabilize some oxidation states, as shown in the case of oxalate that plays a key role in iron speciation [12–14]. Shi et al. [10] concluded that the atmospheric complexation of iron in clouds or rainwater could be essential to describe its global biogeochemical cycles. Furthermore, they suggested that multidisciplinary measurements could provide more realistic formation constants for Fe complexes with organic and inorganic ligands, under conditions relevant to dust aerosol particles. This approach should be followed for all the main chemical species that characterize atmospheric depositions. Within this framework, the goal of the present work is (i) to provide quantitative information about the components of the atmospheric depositions in the Antarctica, and (ii) to propose a chemical model based on the interaction between the main components, with the final target of identifying the key species occurring in wet depositions, or in the soluble fraction of dry depositions. Particular attention was paid to those cations showing bioactivity and/or photo-activity. The results will direct further investigations on the definition of the formation constants of metal complexes, under temperature and ionic strength values that best suit atmospheric processes.

In a project carried out within the National Research Program in the Antarctica (PNRA), entitled “Spatial and temporal (intra- and inter-annual) evolution of the chemical composition of the aerosol in the Victoria Land (Antarctica) in relation with local and long-range transport processes”, atmospheric depositions were collected during the Antarctic summer 2017–2018. Only dry depositions actually occurred in the mentioned period and, therefore, analyses were conducted on the dissolved fraction after dissolution. Some cations were quantified by elemental analysis (Inductively Coupled Plasma—Optical Emission Spectroscopy, ICP-OES, or High Resolution—Inductively Coupled Plasma—Mass Spectroscopy, HR-ICP-MS), whereas anions, main cations, and ammonium were quantified by Ionic Chromatography, IC. The components of the samples considered in the chemical model are: Na^+ , K^+ , NH_4^+ , Ca^{2+} , Mg^{2+} , Cu^{2+} , Mn^{2+} , Zn^{2+} , $\text{Fe}^{2+/3+}$, Cl^- , NO_3^- , SO_4^{2-} , PO_4^{3-} , HCOO^- , and CH_3COO^- , together with the species formed by their interactions. Hydrolytic species of the cations and dissociation constants of the protogenic components were also considered in the model. As a first approximation, the formation constants used here were those defined at 25 °C, because many formation equilibria have not yet been studied at lower temperature. The estimated ionic strength of the samples under study was very low, which allows for the use of thermodynamic formation constants ($T = 298.15 \text{ K}$, $I = 0 \text{ mol L}^{-1}$).

2. Materials and Methods

2.1. Reagents

Chemicals were purchased from Merck KGaA (Darmstadt, Germany) and were of analytical grade. Nitric acid was further purified by sub-boiling distillation in a quartz apparatus, starting from 65% solutions. Water was purified by a Milli-Q system from Merck-Millipore (Darmstadt, Germany), resulting in high-purity water with $18 \text{ M}\Omega \text{ cm}$ re-

sistivity. Intermediate metal standard solutions were prepared from concentrated (1000 and 10,000 mg/L) stock solutions (Sigma-Aldrich TraceCERT, Buchs, Switzerland), and acidified with nitric acid to pH 1.5.

2.2. Sample Collection and Treatment

From November 2017 to January 2018, 13 atmospheric deposition samples were collected by means of passive samplers (sampling bulks). Bulks were placed in eight coastal and continental sites along the Victoria Land, from 73°02' to 74°54' S and westward from the Italian research station "Mario Zucchelli" (MZS). Figure 1 reports the map of Victoria Land, showing the 8 atmospheric deposition sampling sites (MZS, Faraglione Camp, Inexpressible Island, Edmonson Point, Cape King, Cape Phillips, Sarao Point, Mid-Priestley Glacier).

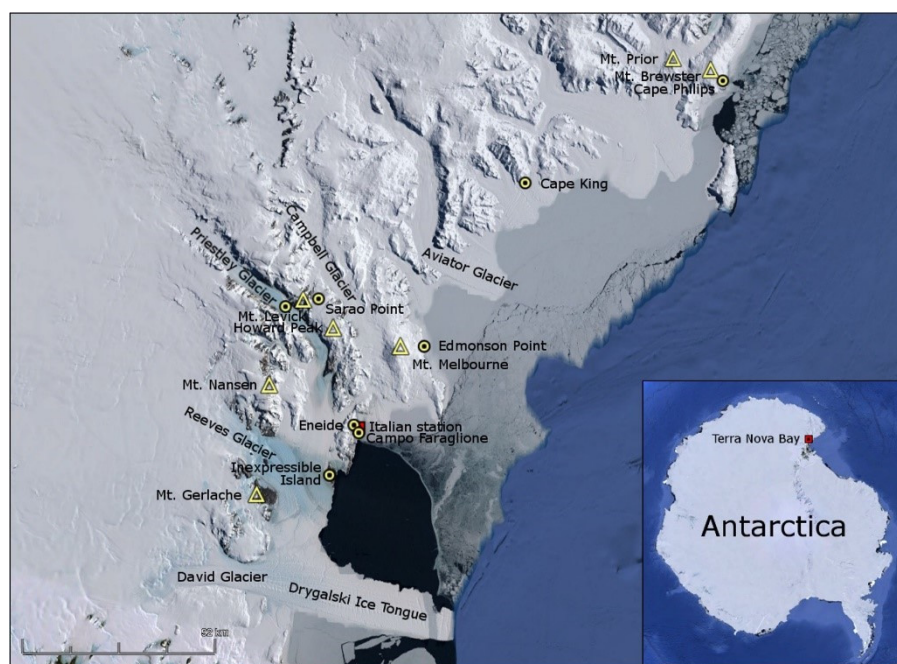


Figure 1. Satellite map of the Victoria Land, showing the position of the Italian Antarctic Station (MZS in the text) and the sampling sites.

Sampling bulks are made of a polyethylene bottle (volume, 10 L) with a polyethylene funnel (volume, ~10 L; surface area = $0.034 \pm 0.002 \text{ m}^2$). Each sampling bulk was placed inside a PVC cylindrical container, specifically modified to ensure the positioning of the bulk funnel at 1.5 m above the ground, avoiding the collection of re-suspended soil particles or drifting snow.

Bulks were removed and replaced after 20–50 days. In addition, sample blanks (hereinafter: field blanks) were also collected in the field, approximately once every month. These blanks were simply placed in the sampling site for 20–30 min and then treated as the deposition samples.

Bulk atmospheric deposition samples were transported to the clean room in MZS at the end of each sampling period, and left at room temperature for a few days. When no wet deposition was collected, 700–900 mL of ultrapure water were added to collect and re-suspend any particles attached to the inner surfaces of the bulk. Subsequently, samples were shaken and vacuum-filtered through $0.45 \mu\text{m}$ membrane filters. All the filtered samples were then frozen at $-20 \text{ }^\circ\text{C}$ until analysis. The collected atmospheric deposition samples, the sampling periods, and the filtration volumes are all reported in Table 1.

Table 1. Sample sites, sampling periods, sampling duration and samples' filtered volumes.

Sample	Site	Sampling Period	Days	Filtered Volume (mL)
D1_1	Mario Zucchelli Station (MZS)	3 November 2017–5 December 2017	32	750
D1_2		5 December 2017–10 January 2018	36	900
D2_1	Faraglione Camp	10 November 2017–30 November 2017	20	750
D2_2		30 November 2017–20 December 2017	20	950
D2_3		20 December 2017–10 January 2018	21	950
D3_1	Edmonson Point	6 November 2017–9 December 2017	33	750
D3_2		9 December 2017–13 January 2018	35	900
D4_1	Inexpressible Island	6 November 2017–9 December 2017	33	1000
D4_2		9 December 2017–10 January 2018	32	900
D5_1	Cape Philips	9 November 2017–29 December 2017	50	900
D6_1	Cape King	9 November 2017–29 December 2017	50	950
D8_1	Sarao Point	18 November 2017–7 January 2018	50	850
D9_1	Priestley Glacier	18 November 2017–7 January 2018	50	1000

2.3. Apparatuses and Procedures

Sample treatments, analyses and decontamination procedures were carried out in clean room laboratories with areas in Class 5 (ISO 14644-1) under laminar flow, both in the Antarctica and in Italy [15]. The used filtration system was the Sulfoflo from Nalgene (Rochester, NY, USA), equipped with 0.45 μm -pore size membrane filters (cellulose mixed esters \varnothing 47 mm, Schleicher & Schuell, Dassel, Germany). Sampling bulks and plastic containers used for storage of sample solutions were of low-density polyethylene material (Kartell, Italy).

For the determination of anions, the atmospheric depositions were analyzed with a Dionex DX 500 Ion Chromatograph, equipped with Rheodyne injector (20 μL sample loop), LC 30 chromatography oven, GP 40 gradient pump, Dionex Ion Pac AG9-HC 4-mm (10–32) guard column, Dionex Ion Pac AS9-HC 4-mm (10–32) anion exchange column, ASRS-ULTRA 4-mm conductivity suppression unit, and ED 40 electrochemical detector, operated in conductivity mode at 30 $^{\circ}\text{C}$. The eluent was a $1.1 \times 10^{-2} \text{ mol L}^{-1} \text{ K}_2\text{CO}_3 / 4.5 \times 10^{-3} \text{ mol L}^{-1} \text{ NaHCO}_3$ mixture, with flow rate of 1.0 mL min^{-1} .

Sodium, potassium, calcium, magnesium, and ammonium cations were analyzed with the same instrument, except that it was equipped with Ion Pac CG12A (4 \times 50 mm) (10–32) guard column, Ion Pac CS12A (4 \times 250 mm) (10–32) cation exchange column, and CSRS-ULTRA 4-mm conductivity suppression unit. The eluent was a $2.0 \times 10^{-2} \text{ mol L}^{-1}$ methanesulfonic acid solution, at a flow rate of 1.0 mL min^{-1} .

Copper, zinc, manganese, and iron cations were quantified according to the concentration levels, by either ICP-OES (Inductively Coupled Plasma—Optical Emission Spectrometer) or HR-ICP-MS (High Resolution—Inductively Coupled Plasma—Mass Spectrometer). In particular, ICP-OES was a Perkin Elmer (Waltham, MA, USA) Optima 7000 DV instrument, equipped with a Mira Mist nebulizer, a cyclonic spray chamber, a dual Échelle monochromator and a dual CCD detector. HR-ICP-MS was a Thermo Fisher Scientific (Waltham, MA, USA) Element 2 instrument, equipped with a conical nebulizer, a Scott spray chamber, a magnetic and electric sector, and a SEM detector. Wavelength, mass resolution, and isotope selection were optimized for each element, to avoid or minimize spectral interferences and to maximize sensitivity. The detection limits (DL) were experimentally determined. The samples were handled in a clean environment under a Class-100 laminar flow bench-hood, to avoid any possible contamination. The reagent blanks were composed of ultra-pure water, acidified with sub-boiling nitric acid (1:1000). The NIST 1640a Certified Reference Material (CRM) was used to validate the measurement procedures by both ICP-OES and HR-ICP-MS. The CRM was an acidified (2% HNO_3) spring water, and it was analyzed either without treatment or diluted, in order to best simulate the concentration levels of real samples. All measurements were performed in triplicate.

Values of field blanks were subtracted from sample concentrations, in order to eliminate contributions from the sampling bulks, transport and storage processes. Because the volumes of the extracts were variable, the concentrations were re-calculated for 1 L of extract.

2.4. Data Processing

The chemical model applied to the atmospheric deposition samples considers the species reported in Tables 2 and 3. The formation constants of the relevant species were derived from literature data (see refs. reported in the two tables). Because all the samples had low ionic strength values, the formation constants selected from the literature were those estimated at quite low ionic strength (see Table 3). If necessary, the Extended Debye–Hückel (EDH) equation [16] was applied to the original literature values, to obtain the $\log K$ values at $I = 0.0 \text{ mol L}^{-1}$ and $t = 25 \text{ }^\circ\text{C}$. These values were used to derive speciation diagrams. Both original and extrapolated values are shown in Tables 2 and 3, with the original experimental conditions indicated as reported in the respective literature. Moreover, because weak interactions between anions and alkaline cations were considered in the chemical model, whenever possible, the selected formation constants were those estimated with non-interacting cations. The species distribution diagrams were drawn using the ES4ECI software [17], which takes into account the possible variation of the ionic strength associated to the variation of the charged species in solution as a function of pH, and corrects the values of the formation constants by applying the EDH equation.

OriginPro 2020 SR1 (by OriginLab Corporation, Northampton, MA, USA) was used for descriptive statistics, data processing, and presentation.

Table 2. Overall ($\log\beta$) and partial ($\log K$) protonation constants of the species considered in the model.

Protonation Constants					
Species	$\log K^a$	$\log\beta^b$	Reference	$\log K$	$\log\beta$
Original Values			Values Estimated by the Application of EDH Equation [16]		
$I = 0 \text{ mol L}^{-1}, t = 25 \text{ }^\circ\text{C}$			$I = 0 \text{ mol L}^{-1}, t = 25 \text{ }^\circ\text{C}$		
HSO_4^-	1.987	1.987	[18]	1.987	1.987
HPO_4^{2-}	12.35	12.35		12.35	12.35
H_2PO_4^-	7.20	19.55	[19]	7.20	19.55
H_3PO_4	2.15	21.70		2.15	21.70
Hac^c	$I = 0 \text{ mol L}^{-1}, \text{NEt}_4\text{I}^e, t = 25 \text{ }^\circ\text{C}$				
	4.74	4.74	[20]	4.74	4.74
Hfor^d	$I = 0.16 \text{ mol}, \text{NEt}_4\text{I}, \text{L}^{-1}, t = 25 \text{ }^\circ\text{C}$				
	3.55	3.55	[21]	3.72	3.72

^a $\log K$ values refer to the general reaction: $\text{H}_{r-1}\text{L}^{z-(r-1)} + \text{H}^+ \rightleftharpoons \text{H}_r\text{L}^{z-r}$, with z = charge of the fully deprotonated ligand; ^b $\log\beta$ values refer to the general reaction: $\text{L}^{z-} + r\text{H}^+ \rightleftharpoons \text{LH}_r^{z-r}$; ^c Hac: acetic acid; ^d Hfor: formic acid; ^e NEt_4I : tetraethylammonium iodide.

Table 3. Overall ($\log\beta$) and partial ($\log K$) formation constants of the species considered in the model.

Formation Constants					
Hydrolytic Species					
Species	$\log K^a$	$\log\beta^b$	Ref.	$\log K$	$\log\beta$
Original Values			Values Estimated by the Application of EDH Equation [16]		
	$I = 0.0 \text{ mol L}^{-1}, t = 25 \text{ }^\circ\text{C}$			$I = 0.0 \text{ mol L}^{-1}, t = 25 \text{ }^\circ\text{C}$	
[CaOH] ⁺	1.3	−12.69		1.3	−12.69
[MgOH] ⁺		−11.44			−11.44
[Mg ₃ (OH) ₄] ⁴⁺		−39.71			−39.71
[CuOH] ⁺		−7.7			−7.7
Cu(OH) ₂		−17.3			−17.3
[Cu(OH) ₃] [−]		−27.8			−27.8
[Cu(OH) ₄] ^{2−}		−39.6			−39.6
[Cu ₂ (OH) ₂] ²⁺		−10.36			−10.36
Cu(OH) ₂ (s)		7.6			7.6
[MnOH] ⁺		−10.59			−10.59
Mn(OH) ₂		−22.2			−22.2
[Mn(OH) ₃] [−]		−34.8			−34.8
[Mn(OH) ₄] ^{2−}		−48.3			−48.3
[Mn ₂ OH] ³⁺		−10.56			−10.56
[Mn ₂ (OH) ₃] ⁺		−23.9	[21]		−23.9
Mn(OH) ₂ (s)		15.2			15.2
[ZnOH] ⁺		−8.96			−8.96
Zn(OH) ₂		−16.9			−16.9
[Zn(OH) ₃] [−]		−28.4			−28.4
[Zn(OH) ₄] ^{2−}		−41.2			−41.2
[Zn ₂ OH] ³⁺		−9.00			−9.00
[Zn ₂ (OH) ₆] ^{2−}		−57.8			−57.8
Zn(OH) ₂ (s)		12.4			12.4
[FeOH] ²⁺		−2.19			−2.19
[Fe(OH) ₂] ⁺		−5.67			−5.67
Fe(OH) ₃		−12.92			−12.92
[Fe(OH) ₄] [−]		−24.4			−24.4
[Fe ₂ (OH) ₂] ⁴⁺		−2.95			−2.95
[Fe ₃ (OH) ₄] ⁵⁺		−6.3			−6.3
Fe(OH) ₃ (s)		3.79			3.79
Complexes and ion pairs					
	$I = 0 \text{ mol L}^{-1}, \text{KCl}, t = 25 \text{ }^\circ\text{C}$			$I = 0 \text{ mol L}^{-1}, t = 25 \text{ }^\circ\text{C}$	
NaCl	−0.30	−0.30		−0.30	−0.30
KCl	−0.27	−0.27		−0.27	−0.27
[CaCl] ⁺	0.57	0.57	[22]	0.57	0.57
[MgCl] ⁺	0.40	0.40		0.40	0.40
	$I = 0 \text{ mol L}^{-1}, \text{NaClO}_4, t = 25 \text{ }^\circ\text{C}$			$I = 0 \text{ mol L}^{-1}, t = 25 \text{ }^\circ\text{C}$	
[CuCl] ⁺	0.83	0.83	[21]	0.83	0.83
CuCl ₂	−0.23	0.60		−0.23	0.60
	$I = 0 \text{ mol L}^{-1}, \text{NaCl}, t = 25 \text{ }^\circ\text{C}$			$I = 0 \text{ mol L}^{-1}, t = 25 \text{ }^\circ\text{C}$	
[ZnCl] ⁺	0.43	0.43		0.43	0.43
ZnCl ₂	0.18	0.61	[21]	0.18	0.61
[ZnCl ₃] [−]	−0.10	0.51		−0.10	0.51
[ZnCl ₄] ^{2−}	−0.31	0.20		−0.31	0.20
[FeCl] ²⁺	1.28	1.28	[23]	1.28	1.28
[FeCl ₂] ⁺	1.16	2.44		1.16	2.44
	$I = 0.16 \text{ mol L}^{-1}, \text{Et}_4\text{NI}, t = 25 \text{ }^\circ\text{C}$			$I = 0 \text{ mol L}^{-1}, t = 25 \text{ }^\circ\text{C}$	
NaH ₂ PO ₄	0.09	18.69			19.78
[NaHPO ₄] [−]	0.69	12.48			13.39
[NaPO ₄] ^{2−}	0.88	0.88	[19]	1.43	1.43
Na ₂ HPO ₄	0.44	12.23			13.32
[Na ₂ PO ₄] [−]	1.68	1.68		2.59	2.59
	$I = 0.16 \text{ mol L}^{-1}, \text{Et}_4\text{NI}^c, t = 25 \text{ }^\circ\text{C}$			$I = 0 \text{ mol L}^{-1}, t = 25 \text{ }^\circ\text{C}$	
KH ₂ PO ₄	0.07	18.67			19.76
[KHPO ₄] [−]	0.50	12.29			13.20
[KPO ₄] ^{2−}	0.81	0.81	[19]	1.36	1.36
K ₂ HPO ₄	0.56	12.35			13.44
[K ₂ PO ₄] [−]	1.28	1.28		2.19	2.19

Table 3. Cont.

Species	Formation Constants			logK	logβ	
	logK ^a	logβ ^b	Ref.			
Original Values			Values Estimated by the Application of EDH Equation [16]			
	<i>I</i> = 0.15 mol L ⁻¹ , KCl, <i>t</i> = 25 °C			<i>I</i> = 0 mol L ⁻¹ , <i>t</i> = 25 °C		
[CaH ₂ PO ₄] ⁺	1.41			1.86	21.41	
CaHPO ₄	2.74		[24]	3.65	16.00	
[CaPO ₄] ⁻	6.46	6.46		7.83	7.83	
	<i>I</i> = 0.2 mol L ⁻¹ , NEt ₄ I, <i>t</i> = 25 °C			<i>I</i> = 0 mol L ⁻¹ , <i>t</i> = 25 °C		
MgHPO ₄	2.41		[25]	2.63	14.98	
	<i>I</i> = 0.1 mol L ⁻¹ , NaClO ₄ , <i>t</i> = 25 °C			<i>I</i> = 0 mol L ⁻¹ , <i>t</i> = 25 °C		
CuHPO ₄		14.93	[21]		16.52	
	<i>I</i> = 0.2 mol L ⁻¹ , NEt ₄ I, <i>t</i> = 25 °C			<i>I</i> = 0 mol L ⁻¹ , <i>t</i> = 25 °C		
MnHPO ₄	2.58		[21]	3.89	16.24	
	<i>I</i> = 0.1 mol L ⁻¹ , NaNO ₃ , <i>t</i> = 25 °C			<i>I</i> = 0 mol L ⁻¹ , <i>t</i> = 25 °C		
ZnHPO ₄	2.4		[21]	3.21	15.56	
	<i>I</i> = 0.1 mol L ⁻¹ , NaClO ₄ , <i>t</i> = 25 °C			<i>I</i> = 0 mol L ⁻¹ , <i>t</i> = 25 °C		
[FeH ₂ PO ₄] ²⁺	3.47		[26]	4.69	24.24	
[FeHPO ₄] ⁺	8.95		[21]	10.17	22.52	
[Fe ₂ HPO ₄] ⁴⁺	6.17			6.77	29.29	
	<i>I</i> = 0.0 mol L ⁻¹ , NEt ₄ I, <i>t</i> = 25 °C			<i>I</i> = 0 mol L ⁻¹ , <i>t</i> = 25 °C		
[NaSO ₄] ⁻	0.65	0.65		0.65	0.65	
[KSO ₄] ⁻	0.75	0.75		0.75	0.75	
CaSO ₄	2.43	2.43		2.43	2.43	
MgSO ₄	2.23	2.23	[27]	2.23	2.23	
CuSO ₄	2.26	2.26		2.26	2.26	
MnSO ₄	2.86	2.86		2.86	2.86	
ZnSO ₄	2.49	2.49		2.49	2.49	
[FeSO ₄] ⁺	4.27	4.27		4.27	4.27	
[Fe(SO ₄) ₂] ⁻	6.11	6.11	[23]	6.11	6.11	
	<i>I</i> = 0.0 mol L ⁻¹ , NEt ₄ I, <i>t</i> = 25 °C			<i>I</i> = 0 mol L ⁻¹ , <i>t</i> = 25 °C		
Na(ac) ^d	-0.11	-0.11	[20]	-0.11	-0.11	
K(ac)	-0.27	-0.27		-0.27	-0.27	
[Ca(ac)] ⁺	1.12	1.12	[28]	1.12	1.12	
[Mg(ac)] ⁺	0.91	0.91	[21]	0.91	0.91	
	<i>I</i> = 0.1 mol L ⁻¹ , NaClO ₄ , <i>t</i> = 25 °C			<i>I</i> = 0 mol L ⁻¹ , <i>t</i> = 25 °C		
[Cu(ac)] ⁺	1.78	1.78	[21]	2.18	2.18	
Cu(ac) ₂	1.02	2.80		1.22	3.40	
	<i>I</i> = 0.1 mol L ⁻¹ , KCl, <i>t</i> = 25 °C			<i>I</i> = 0.1 mol L ⁻¹ , <i>t</i> = 25 °C		
[Mn(ac)] ⁺	0.80	0.80	[21]	1.20	1.20	
	<i>I</i> = 0.1 mol L ⁻¹ , KNO ₃ , <i>t</i> = 25 °C			<i>I</i> = 0 mol L ⁻¹ , <i>t</i> = 25 °C		
[Zn(ac)] ⁺	1.11	1.11	[21]	1.51	1.51	
	<i>I</i> = 0.0 mol L ⁻¹ , NaClO ₄ , <i>t</i> = 25 °C			<i>I</i> = 0 mol L ⁻¹ , <i>t</i> = 25 °C		
[Fe(ac)] ²⁺		4.07			4.07	
[Fe(ac) ₂] ⁺		8.81	[21]		8.81	
[Fe ₃ (OH) ₃ (ac) ₃] ³⁺		11.37			11.37	
	<i>I</i> = 0.03 mol L ⁻¹ , NaCl, <i>t</i> = 25 °C			<i>I</i> = 0 mol L ⁻¹ , <i>t</i> = 25 °C		
[Ca(for)] ⁺ e	0.75	0.75	[21]	1.01	1.01	
[Mg(for)] ⁺	0.75	0.75		1.01	1.01	
	<i>I</i> = 0.1 mol L ⁻¹ , NaNO ₃ , <i>t</i> = 25 °C			<i>I</i> = 0 mol L ⁻¹ , <i>t</i> = 25 °C		
[Cu(for)] ⁺	1.58	1.58	[21]	1.98	1.98	
	<i>I</i> = 0.1 mol L ⁻¹ , KNO ₃ , <i>t</i> = 25 °C			<i>I</i> = 0 mol L ⁻¹ , <i>t</i> = 25 °C		
[Zn(for)] ⁺	1.07	1.07	[21]	1.47	1.47	
	<i>I</i> = 0.0 mol L ⁻¹ , <i>t</i> = 25 °C			<i>I</i> = 0 mol L ⁻¹ , <i>t</i> = 25 °C		
[Fe(for)] ²⁺	3.1	3.1	[8]	3.1	3.1	

^a logK values refer to the general reaction: $pM^{n+} + qH_rL^{z-r} \rightleftharpoons [M_pL_qH_r]^{np+r-qz}$, with *z* = charge of the fully deprotonated ligand; for hydrolytic species the reaction is: $pM^{n+} + qOH^- \rightleftharpoons [M_p(OH)_q]^{np-q}$; ^b logβ values refer to the general reaction: $pM^{n+} + qL^{z-} + rH^+ \rightleftharpoons [M_pL_qH_r]^{np+r-qz}$; for hydrolytic species the reaction is: $pM^{n+} + qH_2O \rightleftharpoons [M_p(OH)_q]^{np-q} + qH^+$; ^c NEt₄I: tetraethylammonium iodide; ^d ac: acetate; ^e for: formate.

3. Results

3.1. Concentrations of the Main Components of Atmospheric Deposition Samples

The main components of the atmospheric deposition samples were quantified by ICP-OES/MS and HPLC-IC. The results, expressed as molar concentration, are collected in

Table 4 and graphically represented in Figures 2 and 3. Estimated recovery percentages from CRM analysis carried out by ICP-OES/MS are between 97.38% and 102.18%. The detailed results are reported in the Supplementary Material file.

The correlation between concentrations of sample components was estimated by using the Pearson coefficients. The results are shown in Table 5, where it is interesting to note the excellent correlation ($R^2 = 0.83\text{--}0.96$) of alkaline and alkaline earth elements with chloride concentration, which suggests a net contribution to all of them by marine aerosol. This is particularly true for samples D1, D3, D4, D5 and D6, which were collected in coastal sites (i.e., MZS, Inexpressible Island, Edmonson Point, Cape Phillips and Cape King, respectively). The marine enrichment factors (MEF) for K^+ , Ca^{2+} , and Mg^{2+} in each sample, i.e., the ratios between their concentrations and that of Na^+ , with respect to the same ratios obtained by considering the mean composition of seawater [29–31], show mean values close to unity (2.4, 2.7, and 1.3, respectively). Therefore, a common and predominantly marine origin for these elements is confirmed. The sample D8-1 was considered as an outlier for the calculation of the mean values previously reported because of its very high MEF values (19.0, 84.1 and 13.8 for K^+ , Ca^{2+} and Mg^{2+} , respectively). This result is largely due to a low Na^+ concentration value. The sampling site D8 (Tourmaline Plateau, Table 4) is located at higher altitude (1621 m a.s.l.) compared to the other sites and, for this reason, it might be less affected by particulate matter of marine origin. However, the non-parametric Kendall's correlation test does not highlight a significant correlation between the MEF values and the altitude of the sampling sites.

The Pearson coefficients show that ammonium, acetate, formate, and zinc are significantly correlated to each other, thereby suggesting a common origin. High concentrations of these ions were recorded at Edmonson Point from mid-summer 2017 (D3). The site is located on the slope of the quiescent volcano Mount Melbourne, and it hosts one of the largest Adélie penguin rookeries in Victoria Land. Several studies highlighted a significant contribution of penguin colonies, together with pack-ice melting, to the release of several organic substances and elements to the above atmosphere. Legrand et al. [32] recorded peaks of acetate and formate in the marine boundary layer at Dumont d'Urville station in January, mainly originating from photochemical degradation of dissolved organic matter, which was released by phytoplankton upon pack-ice melt. The authors also found increasing concentrations of ammonia in summer, also linked to the presence of a large Adélie penguin population from October to March [33,34]. Actually the so-called guano-enriched soils (such as those at Edmonson Point), together with the bacterial decomposition of uric acid, are significant sources of ammonium, oxalate, as well as cations (e.g., potassium and calcium) to the atmospheric aerosol.

Table 4. Concentrations and corresponding standard deviations (SD) (mol L⁻¹) of the components of the atmospheric deposition samples.

Sample Site	Sample	Date	NH ₄ ⁺		Na ⁺		K ⁺		Ca ²⁺		Mg ²⁺		Cu ²⁺		Zn ²⁺		Mn ²⁺	
			Mean	SD	Mean	SD	Mean	SD	Mean	SD	Mean	SD	Mean	SD	Mean	SD	Mean	SD
Mario Zucchelli Station, MZS, AWS Eneide	D1-1	3 November 2017–5 December 2017	3.87×10^{-7}	1.53×10^{-7}	8.43×10^{-5}	4.22×10^{-6}	3.60×10^{-7}	2.67×10^{-7}	6.27×10^{-6}	5.13×10^{-7}	9.60×10^{-6}	1.58×10^{-6}	5.77×10^{-8}	1.14×10^{-9}	1.56×10^{-6}	4.35×10^{-8}	1.85×10^{-8}	1.30×10^{-9}
	D1-2	5 December 2017–10 January 2018	1.89×10^{-6}	2.50×10^{-7}	2.85×10^{-4}	1.28×10^{-5}	1.28×10^{-5}	1.00×10^{-6}	1.89×10^{-5}	1.55×10^{-6}	6.74×10^{-5}	1.09×10^{-5}	1.23×10^{-8}	4.77×10^{-10}	8.95×10^{-7}	3.58×10^{-8}	8.64×10^{-9}	2.17×10^{-10}
Mario Zucchelli Station, MZS, Campo Faraglione	D2-1	10 November 2017–30 November 2017	1.76×10^{-6}	2.94×10^{-7}	2.09×10^{-5}	1.56×10^{-6}	2.99×10^{-6}	4.07×10^{-7}	<LoD	-	8.20×10^{-6}	1.35×10^{-6}	3.43×10^{-8}	8.62×10^{-10}	3.59×10^{-7}	1.18×10^{-8}	4.65×10^{-8}	1.40×10^{-9}
	D2-2	30 November 2017–20 December 2017	4.15×10^{-7}	1.55×10^{-7}	7.58×10^{-6}	4.32×10^{-7}	4.98×10^{-7}	4.43×10^{-8}	8.37×10^{-7}	7.14×10^{-8}	1.04×10^{-6}	1.97×10^{-7}	1.04×10^{-8}	3.78×10^{-10}	1.56×10^{-7}	5.82×10^{-9}	4.68×10^{-9}	6.84×10^{-11}
	D2-3	20 December 2017–10 January 2018	2.03×10^{-6}	3.12×10^{-7}	1.12×10^{-5}	5.86×10^{-7}	1.42×10^{-6}	1.02×10^{-7}	2.50×10^{-6}	2.04×10^{-7}	1.51×10^{-6}	2.72×10^{-7}	2.88×10^{-8}	6.78×10^{-10}	1.87×10^{-7}	7.15×10^{-9}	2.82×10^{-8}	3.75×10^{-10}
Edmonson Point, AWS Penguin	D3-1	6 November 2017–9 December 2017	6.32×10^{-6}	5.72×10^{-7}	1.47×10^{-5}	7.70×10^{-7}	1.71×10^{-6}	1.20×10^{-7}	1.38×10^{-6}	1.13×10^{-7}	2.00×10^{-6}	3.39×10^{-7}	1.36×10^{-8}	2.41×10^{-10}	2.59×10^{-7}	6.17×10^{-9}	7.73×10^{-9}	2.81×10^{-9}
	D3-2	9 December 2017–13 January 2018	6.45×10^{-5}	4.83×10^{-6}	1.47×10^{-4}	6.46×10^{-6}	8.83×10^{-6}	5.71×10^{-7}	1.24×10^{-5}	1.01×10^{-6}	1.80×10^{-5}	2.92×10^{-6}	5.39×10^{-8}	1.46×10^{-9}	9.34×10^{-6}	1.24×10^{-7}	6.15×10^{-8}	2.81×10^{-9}
Inexpressible island, AWS Virginia	D4-1	6 November 2017–9 December 2017	3.45×10^{-7}	1.60×10^{-7}	2.16×10^{-4}	9.85×10^{-6}	6.72×10^{-6}	4.37×10^{-7}	5.11×10^{-6}	4.18×10^{-7}	1.89×10^{-5}	3.06×10^{-6}	2.63×10^{-8}	7.58×10^{-10}	2.68×10^{-7}	1.19×10^{-8}	1.23×10^{-8}	2.02×10^{-10}
	D4-2	9 December 2017–10 January 2018	5.79×10^{-7}	1.74×10^{-7}	2.70×10^{-4}	1.22×10^{-5}	1.04×10^{-5}	6.69×10^{-7}	9.55×10^{-6}	7.81×10^{-7}	2.56×10^{-5}	4.15×10^{-6}	3.06×10^{-8}	1.50×10^{-9}	7.42×10^{-7}	2.86×10^{-8}	2.28×10^{-8}	3.00×10^{-10}
Cape Phillips, AWS Silvia	D5-1	9 November 2017–29 December 2017	2.90×10^{-6}	3.28×10^{-7}	4.40×10^{-5}	2.02×10^{-6}	4.49×10^{-6}	2.96×10^{-7}	6.21×10^{-6}	6.87×10^{-7}	9.05×10^{-6}	1.48×10^{-6}	1.47×10^{-8}	2.35×10^{-10}	1.29×10^{-6}	3.73×10^{-8}	9.20×10^{-9}	1.92×10^{-10}
Cape King, AWS Alessandra	D6-1	9 November 2017–29 December 2017	4.83×10^{-7}	1.68×10^{-7}	3.10×10^{-5}	1.47×10^{-5}	7.30×10^{-6}	4.47×10^{-7}	9.61×10^{-6}	5.08×10^{-7}	3.79×10^{-6}	6.30×10^{-7}	2.98×10^{-8}	9.28×10^{-10}	4.68×10^{-7}	1.55×10^{-8}	4.75×10^{-9}	1.39×10^{-10}
Tourmaline Plateau, AWS Lola	D8-1	18 November 2017–7 January 2018	1.32×10^{-6}	2.21×10^{-7}	1.50×10^{-6}	7.83×10^{-7}	1.04×10^{-6}	7.77×10^{-8}	4.85×10^{-6}	3.97×10^{-7}	2.44×10^{-6}	4.12×10^{-7}	2.65×10^{-8}	1.01×10^{-9}	6.38×10^{-7}	2.31×10^{-8}	9.62×10^{-9}	1.30×10^{-10}
Priestley Glacier, AWS Zoraida	D9-1	18 November 2017–7 January 2018	6.80×10^{-7}	1.80×10^{-7}	5.86×10^{-5}	2.65×10^{-6}	5.58×10^{-6}	3.65×10^{-7}	4.92×10^{-6}	4.02×10^{-7}	6.26×10^{-6}	1.03×10^{-6}	4.48×10^{-8}	6.61×10^{-10}	1.29×10^{-6}	6.53×10^{-8}	7.43×10^{-8}	2.81×10^{-9}

Table 4. Cont.

			Fe ^{2+/3+}		Cl ⁻		NO ₃ ⁻		SO ₄ ²⁻		PO ₃ ³⁻		HCOO ⁻		CH ₃ COO ⁻	
			Mean	SD	Mean	SD	Mean	SD	Mean	SD	Mean	SD	Mean	SD	Mean	SD
Mario Zucchelli Station, MZS, AWS Eneide	D1-1	3 November 2017-5 December 2017	4.03 × 10 ⁻⁸	2.21 × 10 ⁻⁹	7.43 × 10 ⁻⁵	6.38 × 10 ⁻⁶	1.76 × 10 ⁻⁵	2.20 × 10 ⁻⁶	1.43 × 10 ⁻⁵	1.48 × 10 ⁻⁶	1.09 × 10 ⁻⁶	4.59 × 10 ⁻⁷	4.81 × 10 ⁻⁷	4.88 × 10 ⁻⁸	4.43 × 10 ⁻⁷	5.96 × 10 ⁻⁸
	D1-2	5 December 2017-10 January 2018	8.22 × 10 ⁻⁹	4.03 × 10 ⁻¹⁰	3.93 × 10 ⁻⁴	2.98 × 10 ⁻⁵	4.70 × 10 ⁻⁶	8.60 × 10 ⁻⁷	1.26 × 10 ⁻⁵	1.31 × 10 ⁻⁶	9.23 × 10 ⁻⁷	4.12 × 10 ⁻⁷	6.51 × 10 ⁻⁶	6.60 × 10 ⁻⁷	1.17 × 10 ⁻⁶	1.57 × 10 ⁻⁷
Mario Zucchelli Station, MZS, Campo Faraglione	D2-1	10 November 2017-30 November 2017	1.79 × 10 ⁻¹²	1.80 × 10 ⁻¹²	7.65 × 10 ⁻⁶	1.66 × 10 ⁻⁶	1.58 × 10 ⁻⁵	2.02 × 10 ⁻⁶	1.43 × 10 ⁻⁵	1.48 × 10 ⁻⁶	4.27 × 10 ⁻⁷	1.28 × 10 ⁻⁷	5.57 × 10 ⁻⁷	1.44 × 10 ⁻⁷	<LoD	-
	D2-2	30 November 2017-20 December 2017	9.15 × 10 ⁻⁹	1.79 × 10 ⁻¹⁰	2.65 × 10 ⁻⁶	1.36 × 10 ⁻⁶	1.98 × 10 ⁻⁶	5.97 × 10 ⁻⁷	8.40 × 10 ⁻⁷	1.58 × 10 ⁻⁷	7.85 × 10 ⁻⁷	2.35 × 10 ⁻⁷	2.00 × 10 ⁻⁶	2.81 × 10 ⁻⁷	8.60 × 10 ⁻⁷	1.16 × 10 ⁻⁷
	D2-3	20 December 2017-10 January 2018	3.39 × 10 ⁻⁹	1.02 × 10 ⁻¹⁰	4.38 × 10 ⁻⁶	1.46 × 10 ⁻⁶	2.76 × 10 ⁻⁶	2.95 × 10 ⁻⁷	1.77 × 10 ⁻⁶	2.45 × 10 ⁻⁷	2.55 × 10 ⁻⁶	7.62 × 10 ⁻⁷	1.81 × 10 ⁻⁶	2.63 × 10 ⁻⁷	9.86 × 10 ⁻⁷	1.33 × 10 ⁻⁷
Edmonson Point, AWS Penguin	D3-1	6 November 2017-9 December 2017	3.09 × 10 ⁻⁸	7.09 × 10 ⁻¹⁰	1.35 × 10 ⁻⁵	1.30 × 10 ⁻⁶	9.24 × 10 ⁻⁶	1.32 × 10 ⁻⁶	3.79 × 10 ⁻⁶	3.76 × 10 ⁻⁷	1.39 × 10 ⁻⁶	7.28 × 10 ⁻⁷	4.44 × 10 ⁻⁷	1.01 × 10 ⁻⁷	4.42 × 10 ⁻⁷	5.95 × 10 ⁻⁸
	D3-2	09 December 2017-13 January 2018	4.64 × 10 ⁻⁹	1.67 × 10 ⁻¹⁰	2.04 × 10 ⁻⁴	1.53 × 10 ⁻⁵	6.34 × 10 ⁻⁶	1.02 × 10 ⁻⁶	1.17 × 10 ⁻⁵	1.16 × 10 ⁻⁶	1.46 × 10 ⁻⁶	7.47 × 10 ⁻⁷	2.95 × 10 ⁻⁵	3.03 × 10 ⁻⁶	5.67 × 10 ⁻⁶	7.64 × 10 ⁻⁷
Inexpressible island, AWS Virginia	D4-1	6 November 2017-9 December 2017	3.97 × 10 ⁻⁸	1.17 × 10 ⁻⁹	1.85 × 10 ⁻⁴	1.39 × 10 ⁻⁵	1.41 × 10 ⁻⁵	1.83 × 10 ⁻⁶	2.40 × 10 ⁻⁵	3.59 × 10 ⁻⁶	6.53 × 10 ⁻⁷	5.27 × 10 ⁻⁷	7.87 × 10 ⁻⁷	1.33 × 10 ⁻⁷	<LoD	-
	D4-2	9 December 2017-10 January 2018	9.05 × 10 ⁻⁸	2.60 × 10 ⁻⁹	2.60 × 10 ⁻⁴	1.94 × 10 ⁻⁵	1.18 × 10 ⁻⁵	1.59 × 10 ⁻⁶	3.14 × 10 ⁻⁵	4.30 × 10 ⁻⁶	9.81 × 10 ⁻⁷	6.15 × 10 ⁻⁷	4.34 × 10 ⁻⁶	4.87 × 10 ⁻⁷	8.54 × 10 ⁻⁷	1.15 × 10 ⁻⁷
Cape Phillips, AWS Silvia	D5-1	9 November 2017-29 December 2017	1.58 × 10 ⁻⁸	7.35 × 10 ⁻¹⁰	3.60 × 10 ⁻⁵	2.94 × 10 ⁻⁶	4.20 × 10 ⁻⁶	8.10 × 10 ⁻⁷	7.48 × 10 ⁻⁶	7.64 × 10 ⁻⁷	<LoD	-	1.94 × 10 ⁻⁶	2.47 × 10 ⁻⁷	<LoD	-
Cape King, AWS Alessandra	D6-1	9 November 2017-29 December 2017	1.33 × 10 ⁻⁷	3.19 × 10 ⁻⁹	8.83 × 10 ⁻⁶	9.74 × 10 ⁻⁷	1.95 × 10 ⁻⁶	5.94 × 10 ⁻⁷	1.50 × 10 ⁻⁶	1.72 × 10 ⁻⁷	4.98 × 10 ⁻⁷	4.88 × 10 ⁻⁷	3.80 × 10 ⁻⁶	4.33 × 10 ⁻⁷	<LoD	-
Tourmaline Plateau, AWS Lola	D8-1	18 November 2017-7 January 2018	3.70 × 10 ⁻⁸	1.13 × 10 ⁻⁹	1.38 × 10 ⁻⁵	1.33 × 10 ⁻⁶	9.60 × 10 ⁻⁶	1.36 × 10 ⁻⁶	4.22 × 10 ⁻⁶	4.41 × 10 ⁻⁷	4.11 × 10 ⁻⁷	1.23 × 10 ⁻⁷	2.15 × 10 ⁻⁶	2.89 × 10 ⁻⁷	7.13 × 10 ⁻⁶	7.69 × 10 ⁻⁷
Priestley Glacier, AWS Zoraida	D9-1	18 November 2017-7 January 2018	1.76 × 10 ⁻⁷	4.71 × 10 ⁻⁹	5.24 × 10 ⁻⁵	4.15 × 10 ⁻⁶	contaminated	2.60 × 10 ⁻⁴	3.14 × 10 ⁻⁵	3.13 × 10 ⁻⁶	1.18 × 10 ⁻⁶	6.68 × 10 ⁻⁷	<LoD	-	2.59 × 10 ⁻⁶	3.11 × 10 ⁻⁷

Table 5. Pearson correlation coefficients. The significant correlation coefficients at 0.05 level are shown in bold.

Component	Na ⁺	K ⁺	Mg ²⁺	Ca ²⁺	NH ₄ ⁺	Cu ²⁺	Zn ²⁺	Mn ²⁺	Fe ^{2+/3+}	Cl ⁻	NO ₃ ⁻	PO ₄ ³⁻	SO ₄ ²⁻	CH ₃ COO ⁻	HCOO ⁻
Na ⁺	1	0.83496	0.85058	0.73952	0.13495	0.03075	0.19082	-0.00877	0.01639	0.96584	0.20302	-0.01825	0.61123	0.1717	0.24807
K ⁺	0.83496	1	0.79604	0.84632	0.26964	-0.01455	0.30855	0.13602	0.21988	0.85312	-0.14672	-0.09359	0.47104	0.22277	0.40537
Mg ²⁺	0.85058	0.79604	1	0.82956	0.06904	-0.16433	0.11584	-0.08319	-0.15745	0.93309	-0.0052	-0.05421	0.31679	0.14133	0.20868
Ca ²⁺	0.73952	0.84632	0.82956	1	0.32443	0.08058	0.40661	-0.02796	0.08011	0.83233	-0.2185	-0.04494	0.19156	0.38413	0.50374
NH ₄ ⁺	0.13495	0.26964	0.06904	0.32443	1	0.43951	0.97435	0.47838	-0.25164	0.24096	-0.12378	0.25762	-0.04962	0.90797	0.94887
Cu ²⁺	0.03075	-0.01455	-0.16433	0.08058	0.43951	1	0.55576	0.67104	0.27734	-7.705 × 10 ⁻⁴	0.50054	0.25044	0.39146	0.35521	0.40053
Zn ²⁺	0.19082	0.30855	0.11584	0.40661	0.97435	0.55576	1	0.53132	-0.1587	0.2899	-0.06491	0.19431	0.059	0.88501	0.94694
Mn ²⁺	-0.00877	0.13602	-0.08319	-0.02796	0.47838	0.67104	0.53132	1	0.28198	0.02015	0.25531	0.3152	0.5116	0.33808	0.42464
Fe ^{2+/3+}	0.01639	0.21988	-0.15745	0.08011	-0.25164	0.27734	-0.1587	0.28198	1	-0.08359	-0.01898	-0.09171	0.48489	-0.32708	-0.17131
Cl ⁻	0.96584	0.85312	0.93309	0.83233	0.24096	-7.705 × 10 ⁻⁴	0.2899	0.02015	-0.08359	1	0.0821	0.03379	0.4828	0.30039	0.36719
NO ₃ ⁻	0.20302	-0.14672	-0.0052	-0.2185	-0.12378	0.50054	-0.06491	0.25531	-0.01898	0.0821	1	-0.16151	0.63613	-0.17001	-0.20501
PO ₄ ³⁻	-0.01825	-0.09359	-0.05421	-0.04494	0.25762	0.25044	0.19431	0.3152	-0.09171	0.03379	-0.16151	1	-0.05452	0.2901	0.17846
SO ₄ ²⁻	0.61123	0.47104	0.31679	0.19156	-0.04962	0.39146	0.059	0.5116	0.48489	0.4828	0.63613	-0.05452	1	-0.13284	-0.02322
CH ₃ COO ⁻	0.1717	0.22277	0.14133	0.38413	0.90797	0.35521	0.88501	0.33808	-0.32708	0.30039	-0.17001	0.2901	-0.13284	1	0.95727
HCOO ⁻	0.24807	0.40537	0.20868	0.50374	0.94887	0.40053	0.94694	0.42464	-0.17131	0.36719	-0.20501	0.17846	-0.02322	0.95727	1

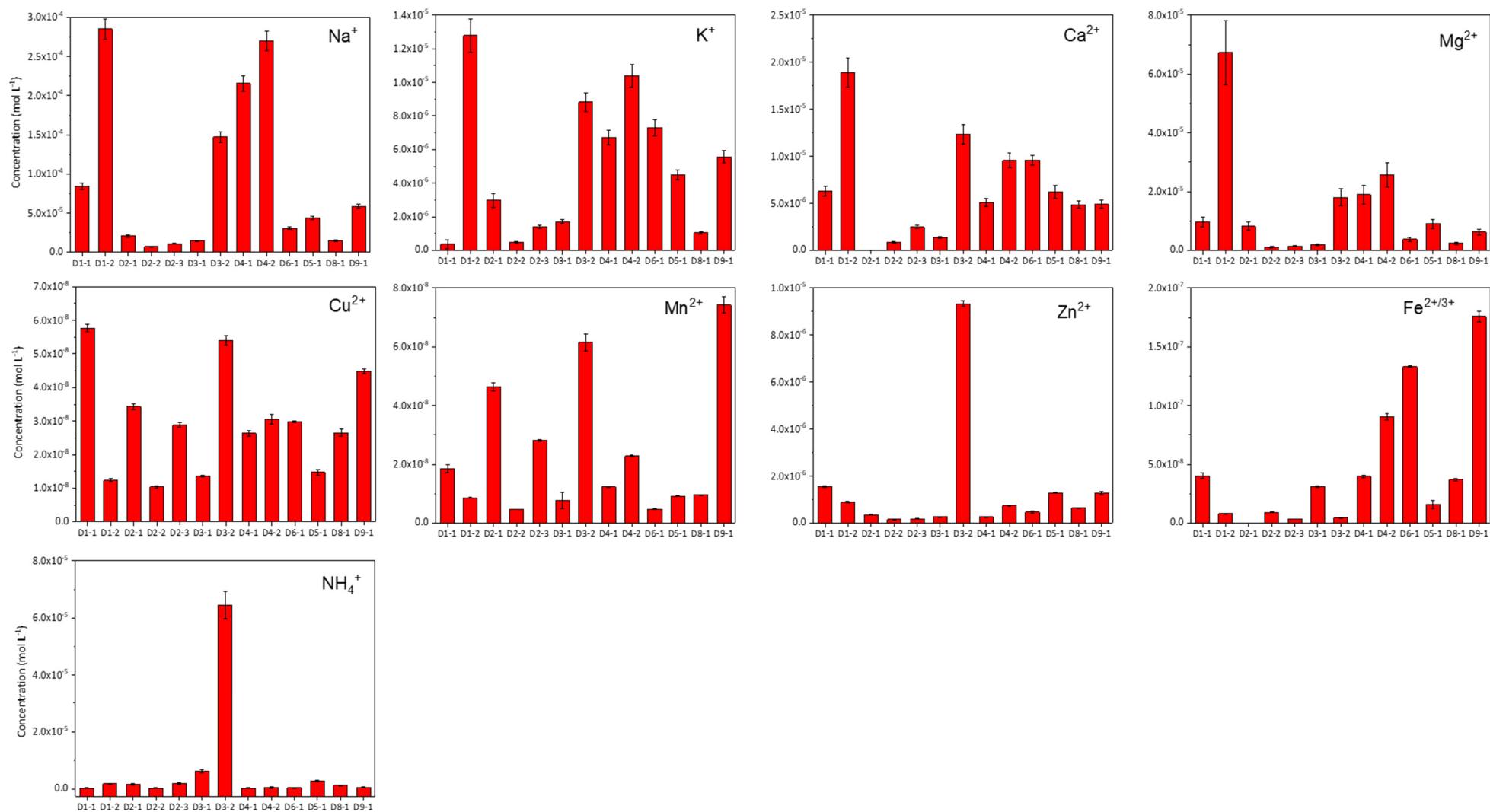


Figure 2. Concentrations and corresponding standard deviations (mol L⁻¹) of the cations of the atmospheric deposition samples. The horizontal axis labels represent the sample codes (see Table 1).

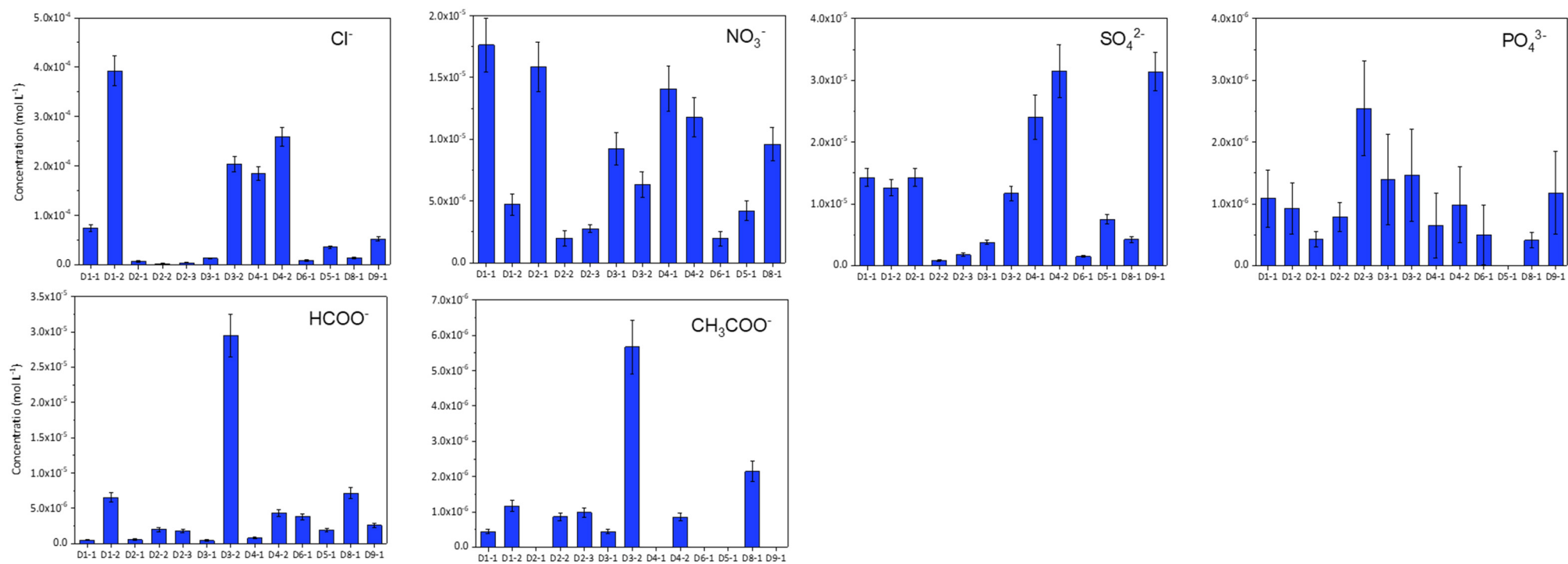
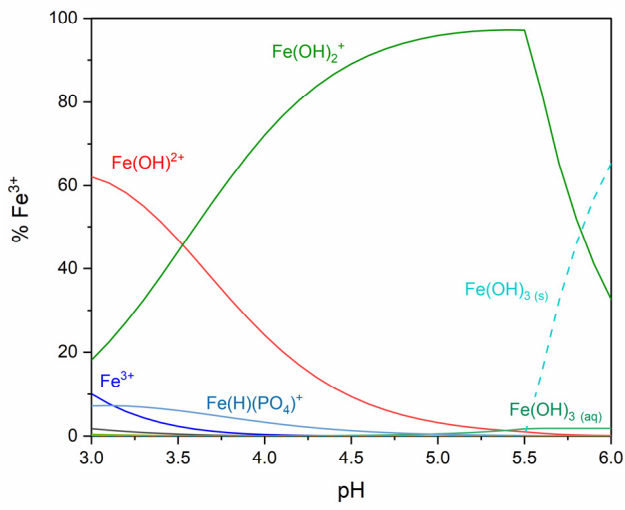


Figure 3. Concentrations and corresponding standard deviations (mol L⁻¹) of the anions of the atmospheric deposition samples. The horizontal axis labels represent the sample codes (see Table 1).

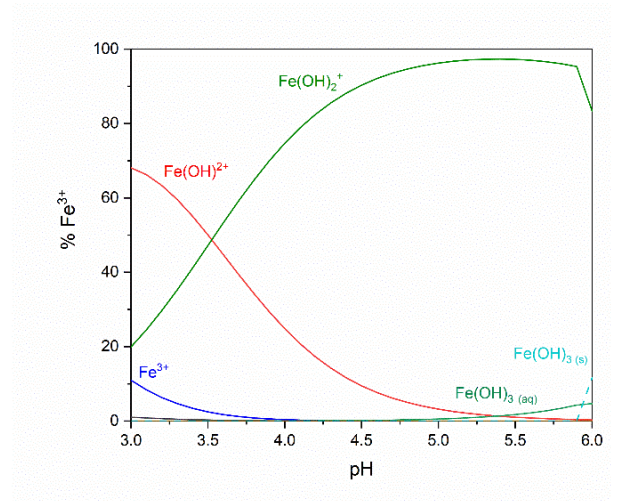
3.2. Speciation of the Main Components of Atmospheric Deposition Samples

The application to the atmospheric deposition samples of a chemical model, which considers the species listed in Tables 1 and 2, allowed us to draw species distribution diagrams as a function of pH. Iron was considered as Fe(III) supposing a complete oxidation of Fe(II) during the collection and storage of the samples. The speciation distribution diagrams were drawn for each sample in the pH range 3–6, which was chosen to be representative of rainwater pH. The diagrams show that most cations would occur as aquoions in the whole pH range, while Fe(III) would occur as hydrolytic forms. The results obtained by plotting the percentage of Fe(III) occurring as different species for three different samples (D1-1, D5-1 and D3-2) are shown in Figure 4a–c. The three samples under consideration are characterized by different concentration levels of total iron, namely $4.03 \times 10^{-8} \text{ mol L}^{-1}$ (D1-1), $1.58 \times 10^{-8} \text{ mol L}^{-1}$ (D5-1) and $4.64 \times 10^{-9} \text{ mol L}^{-1}$ (D3-2). The formation of the solid species $\text{Fe}(\text{OH})_3(s)$ seems to be related to the concentration of Fe(III) in solution (the higher the $[\text{Fe}(\text{III})]$, the more $\text{Fe}(\text{OH})_3(s)$ is formed). The presence of complexes with organic acids is negligible at the concentration levels found in the samples, whereas the hydrolysis equilibria are predominant. However, one should consider that this finding applies to samples obtained by dissolution of solid depositions in a quite high water volume (see experimental section), which is poorly representative of chemical equilibria that may take place on deliquescent atmospheric particles.

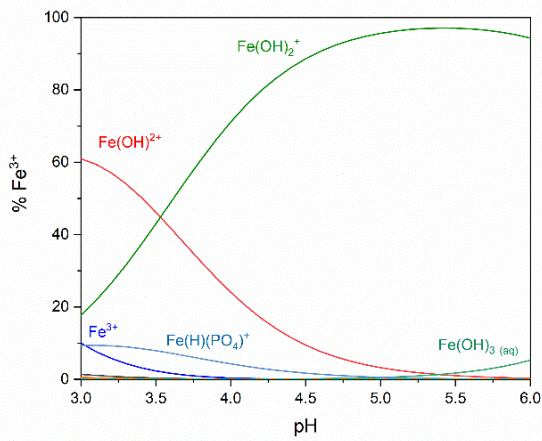
Therefore, further application of the chemical model was devoted to the understanding of what would happen by increasing the component concentration (i.e., a scenario of components dissolution in much lesser water volume), as it may be the case of a thin water film covering deliquescent atmospheric particles, which happens when the particles act as cloud condensation nuclei (CCN) in the atmosphere. A multiplicative factor was thus applied to all the original concentration values in the extraction water, thereby ensuring that the concentration increase would maintain constant ratios between the components. By so doing, the role of inorganic and organic ligands became evident. An example of this behavior is shown for Cu(II) (see Figure 5a,b). Speciation diagrams were thus built by multiplying the components concentrations of the samples D1-1 and D3-2 by 10, 100, and 1000 times (multiplicative factors as per the above discussion). Samples D1-1 and D3-2 were initially chosen for this test, because they are characterized by quite different composition. In particular, sample D3-2 shows high concentration values of ammonium, acetate, formate, and zinc, as highlighted above. Figure 6 shows the percentage of the free cations of each element, which would occur in solution as a function of the concentration levels of the solution components (i.e., detected concentrations times the multiplicative factors), obtained from speciation diagrams. For cations with charge 2, one observes a quite evident decrease of the percentage of the dissolved free cation as a function of the component concentration, while alkaline ions are less sensitive to concentration changes. Fe is not displayed in the figure, because it is predominantly present as hydroxy species or in complexed form. Figures 7 and 8 show the percentages of cations involved in the different chemical forms, as a function of the concentration level of the components (multiplicative factors) at pH = 6.0. In the case of sample D1-1 (Figure 7) one observes important roles of the inorganic anions (chloride, sulfate, and hydrogen phosphate) in complex formation with all the cations, while organic acids such as acetate and formate play quite negligible roles. At pH = 6.0, Fe(III) is in the solid form. The lack of free Fe in solution can have some environmental consequences, e.g., it would slow down the oxidative removal of organic species (natural compounds and pollutants) that can be present in the thin water film when PM acts as CCN, thereby reducing the efficiency of those chemical and photochemical processes that are based on the catalytic behavior of Fe (e.g., Fenton reactions) [35]. In the case of sample D3-2 (Figure 8), the speciation of Ca, Mg, Cu and Zn is quite different, because of a non-negligible contribution of the organic acids to the coordination of metal cations.



(a)



(b)



(c)

Figure 4. Species of Fe(III) occurring in the soluble fraction of the atmospheric deposition samples as a function of pH: (a) sample D1-1; (b) sample D5-1; (c) sample D3-2.

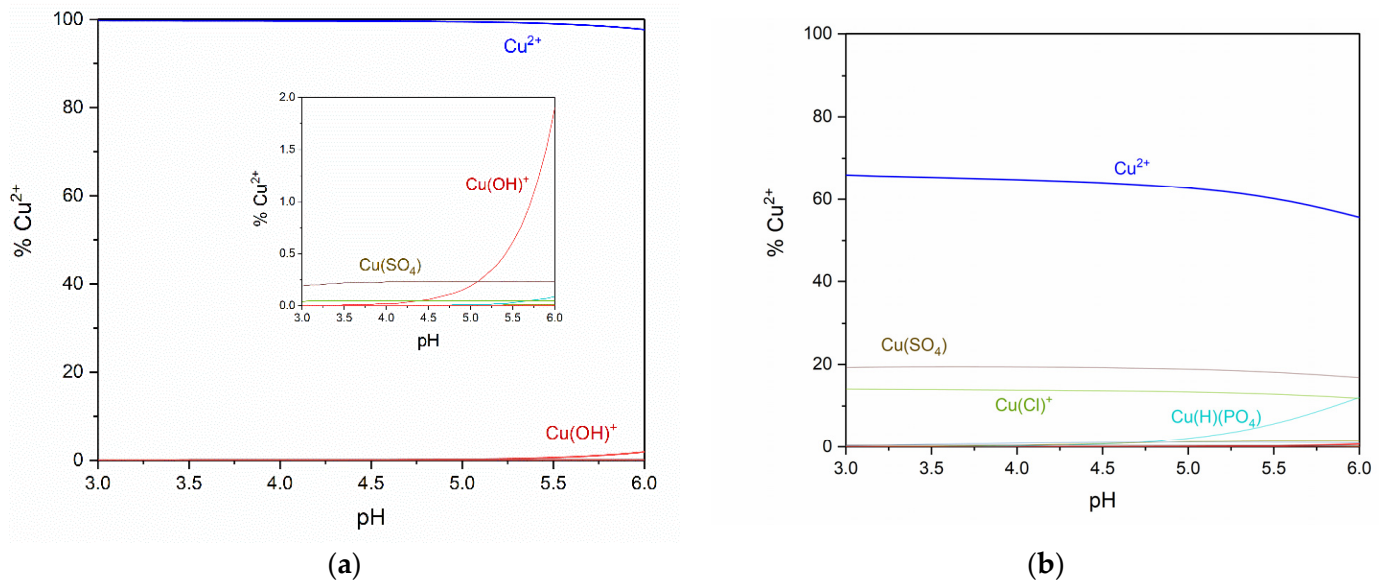


Figure 5. Species of Cu(II) occurring in the soluble fraction of the atmospheric deposition sample D1-1, as a function of pH: (a) sample D1-1 (the inset graph shows the species distribution with an enlarged scale); (b) sample D1-1, with concentration increased by a factor 10³.

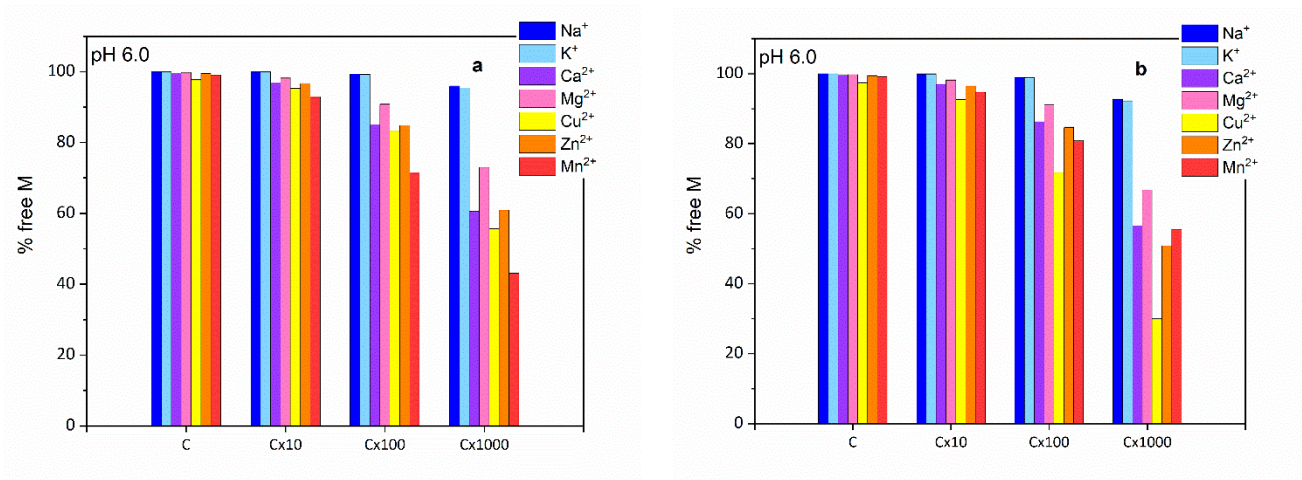


Figure 6. Percentages of free cations in solution, as a function of the concentration level of the components, at pH 6.0. Here, the concentrations of the atmospheric deposition sample D1-1 (a) and D3-2 (b) are those determined in deposition samples (C) or multiplied by a factor 10, 100, or 1000.

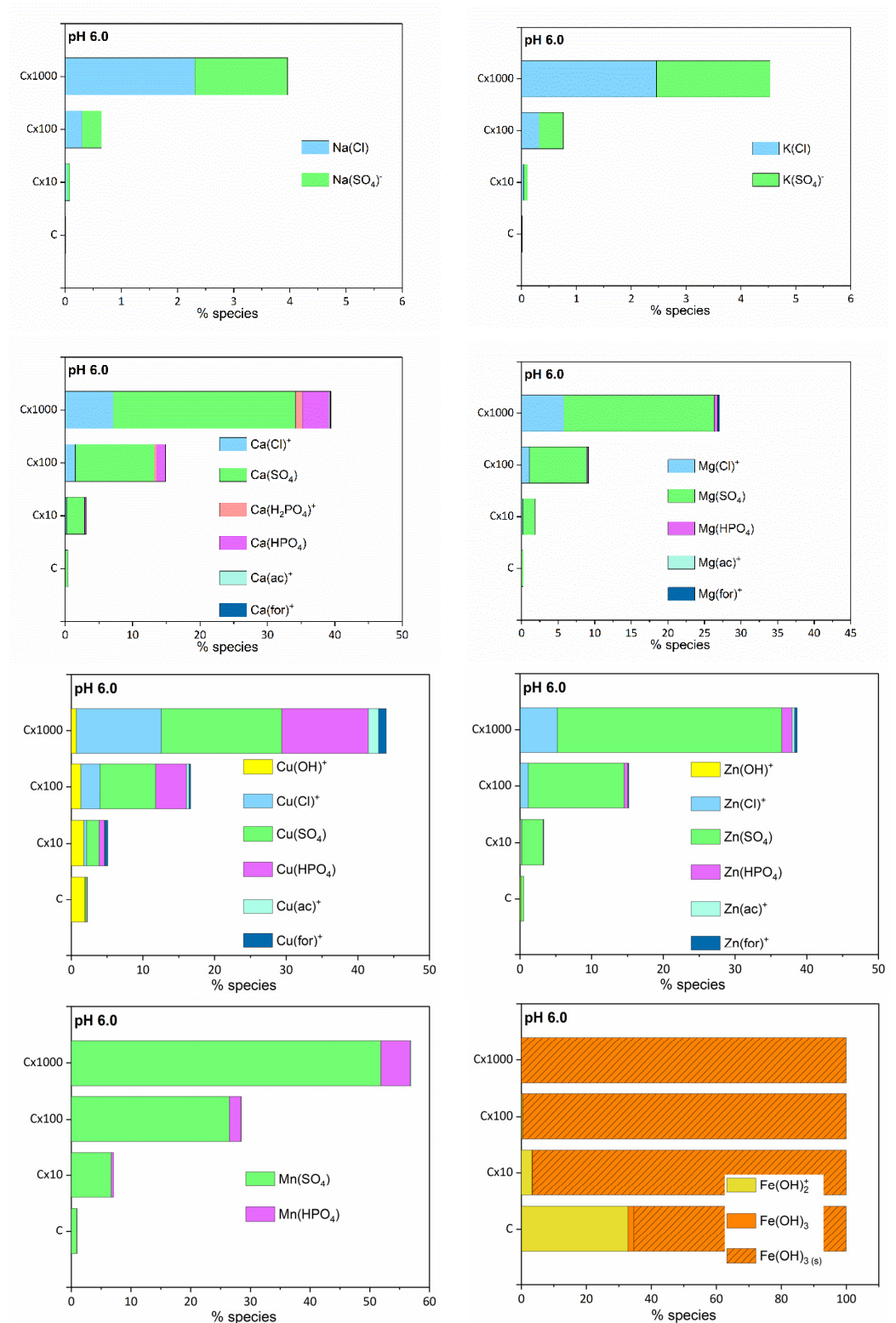


Figure 7. Percentages of cations involved in the different species, as a function of the concentration level of the components, at pH 6.0. The concentrations are those of the atmospheric deposition sample D1-1 (C) or the same multiplied by a factor 10, 100, or 1000.

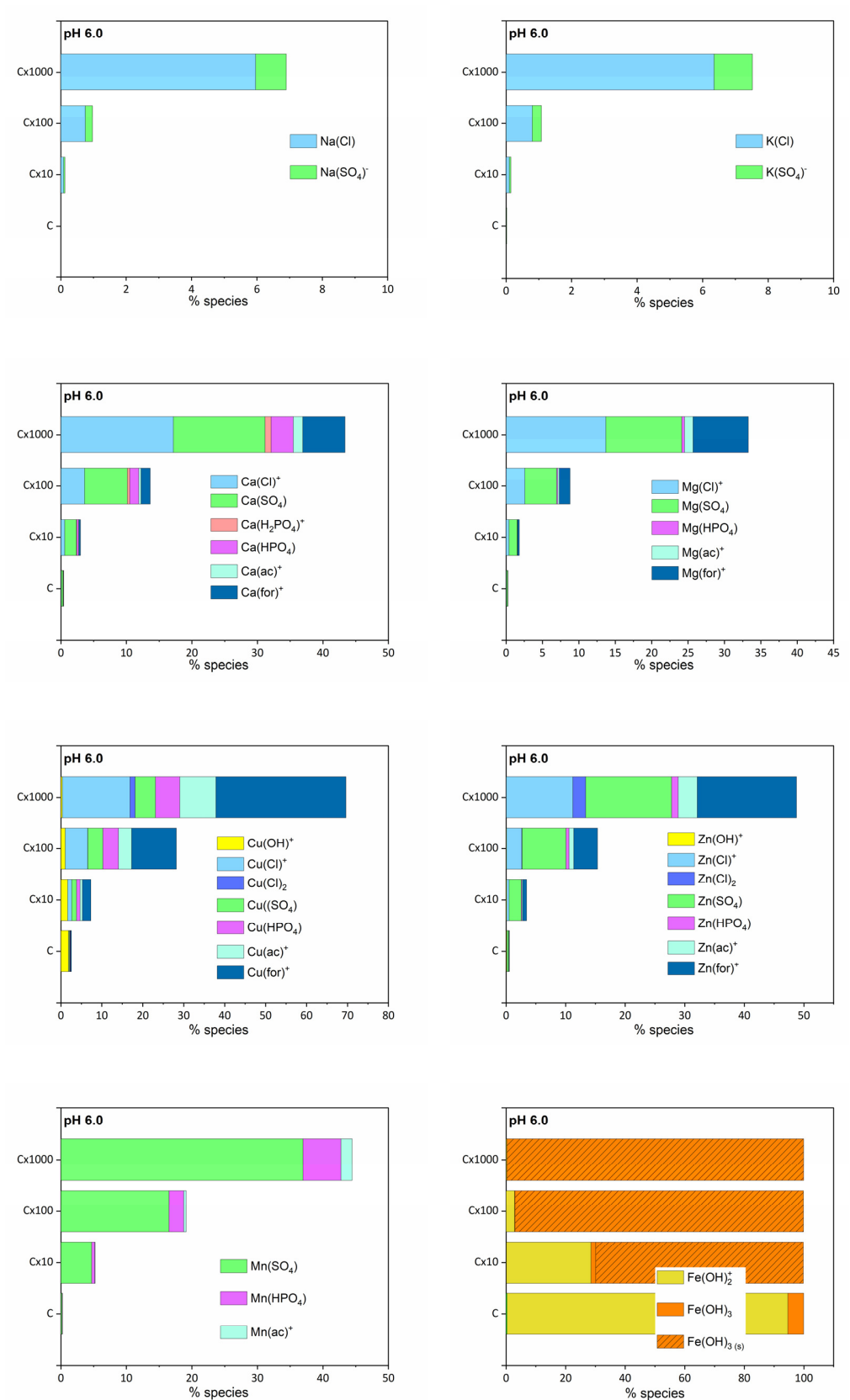


Figure 8. Percentages of cations involved in the different species as a function of the concentration level of the components, at pH 6.0. The concentrations are those of the atmospheric deposition sample D3-2 (C), or the same multiplied by a factor 10, 100, or 1000.

4. Conclusions

The main ionic components were quantified in atmospheric depositions collected at eight sites located in Victoria Land during the Antarctic summer 2017–2018. The main inorganic cations in particulate matter aqueous extracts are represented by alkali and alkaline earth ions, and ammonium. The correlations between some components' concentrations suggest that the marine aerosol strongly affected the composition of the atmospheric depositions, as expected by the location of the sites. Moreover, there was a peculiarity in samples from Edmonson Point (D3), which were characterized by high concentrations of ammonium, acetate, formate, and zinc, probably due to the presence of an Adélie penguin rookery near the sampling site.

A chemical model, based on the interaction between the main components, was proposed and applied to the samples to identify the main species occurring in atmospheric depositions. It was possible to draw the species distribution diagrams as a function of pH, and to foresee the effect of an increase in the concentration level of all the solution components, which simulates what could happen when the particles act as cloud condensation nuclei (CCN) in the atmosphere and, therefore, a thin water film covers the atmospheric particles in the process.

Among transition metals, only Cu, Fe, Mn, and Zn were present in significant concentrations. The speciation study showed that most cations occurred as aquoions over the whole pH range, except for Fe that occurred predominantly as hydrolytic forms. The anions detected in the aqueous extract had a scarce influence on element speciation, due to their low concentrations. The roles of inorganic anions such as chloride, sulfate and hydrogen phosphate only became important when increasing the concentrations of the components by a factor >100, while the presence of organic acids such as acetate and formate gained significance only for samples where concentrations were higher than 10^{-5} mol L⁻¹.

As mentioned before, the results presented here are a first approximation of the chemical speciation of the real samples, because the formation constants used here are defined at 25 °C, while temperatures in the coastal Antarctic area are much lower even during summer, when water anyway occurs in the liquid phase on deliquescent particles. Still, we could identify the chemical equilibria that mostly affect the chemical system. First of all, the hydrolytic species of the cations play a key role such as, most notably, in the case of Fe(III). Furthermore, sulfate is the inorganic anion mostly involved in the formation of complexes, while organic acids would be relevant only for some samples.

Future studies will need to tackle the measurement of the formation constants of these species, together with the related protonation constants of the ligands, at low temperatures and at different ionic strengths, to improve the modeling capacity. The results of such studies will enable researchers to gain insight into the behavior of metals in wet depositions, which is fundamental knowledge to drive atmospheric photochemistry studies and to model biogeochemical cycles of metal cations.

Supplementary Materials: The following supporting information can be downloaded at: <https://www.mdpi.com/article/10.3390/app12094438/s1>.

Author Contributions: Conceptualization, S.B. (Silvia Berto), M.M. (Mery Malandrino), D.V. and S.I.; methodology, S.B. (Silvia Berto), S.B. (Stefano Bertinetti), S.I., M.M. (Mery Malandrino) and D.V.; software and formal analysis, S.B. (Silvia Berto); investigation, S.B. (Stefano Bertinetti), E.C. and S.I.; resources, D.V., M.M. (Mery Malandrino), A.A. and C.T.; data curation, S.B. (Silvia Berto), M.M. (Mery Malandrino), E.C. and M.M. (Matteo Marafante); writing—original draft preparation, S.B. (Silvia Berto) and S.B. (Stefano Bertinetti); writing—review and editing, S.B. (Silvia Berto), S.B. (Stefano Bertinetti), O.A., D.V. and S.I.; visualization, S.B. (Silvia Berto) and M.M. (Matteo Marafante); supervision, project administration and funding acquisition, S.I. and D.V. All authors have read and agreed to the published version of the manuscript.

Funding: This research was financially supported by the MIUR/PNRA program in the framework of the PNRA project PNRA2014_0026 entitled "Spatial and temporal (intra- and inter-annual) evolution

of the chemical composition of the aerosol in the Victoria Land (Antarctica) in relation with local and long-range transport processes”.

Institutional Review Board Statement: Not applicable.

Informed Consent Statement: Not applicable.

Data Availability Statement: Data is contained within the article.

Acknowledgments: The authors gratefully acknowledge National Agency for New Technologies, Energy and Sustainable Economic Development (ENEA) for logistic support.

Conflicts of Interest: The authors declare no conflict of interest.

References

1. Jickells, T.D.; An, Z.S.; Andersen, K.K.; Baker, A.R.; Bergametti, G.; Brooks, N.; Cao, J.J.; Boyd, P.W.; Duce, R.A.; Hunter, K.A.; et al. Global Iron Connections Between Desert Dust, Ocean Biogeochemistry, and Climate. *Science* **2005**, *308*, 67–71. [[CrossRef](#)]
2. Henderson, G.; Anderson, R.; Adkins, J.; Andersson, P.; Boyle, E.A.; Cutter, G.; De Baar, H.J.W.; Eisenhauer, A.; Frank, M.; Francois, R.; et al. GEOTRACES An international study of the global marine biogeochemical cycles of trace elements and their isotopes. *Geochemistry* **2007**, *67*, 85–131. [[CrossRef](#)]
3. Sarthou, G.; Baker, A.R.; Blain, S.; Achterberg, E.P.; Boye, M.; Bowie, A.R.; Croot, P.; Laan, P.; de Baar, H.J.; Jickells, T.D.; et al. Atmospheric iron deposition and sea-surface dissolved iron concentrations in the eastern Atlantic Ocean. *Deep Sea Res. Part I Oceanogr. Res. Pap.* **2003**, *50*, 1339–1352. [[CrossRef](#)]
4. Martin, J.H.; Gordon, R.M.; Fitzwater, S.E.; Martin, H.; Gordon, R.M.; Fitzwater, S.E. Iron limitation? *Limnol. Oceanogr.* **1991**, *36*, 1793–1802. [[CrossRef](#)]
5. Meskhidze, N.; Nenes, A.; Chameides, W.L.; Luo, C.; Mahowald, N. Atlantic Southern Ocean productivity: Fertilization from above or below? *Glob. Biogeochem. Cycles* **2007**, *21*, GB2006. [[CrossRef](#)]
6. Tagliabue, A.; Bopp, L.; Aumont, O. Evaluating the importance of atmospheric and sedimentary iron sources to Southern Ocean biogeochemistry. *Geophys. Res. Lett.* **2009**, *36*, L13601. [[CrossRef](#)]
7. Struve, T.; Pahnke, K.; Lamy, F.; Wengler, M.; Böning, P.; Winckler, G. A circumpolar dust conveyor in the glacial Southern Ocean. *Nat. Commun.* **2020**, *11*, 1–11. [[CrossRef](#)]
8. Paris, R.; Desboeufs, K.V. Effect of atmospheric organic complexation on iron-bearing dust solubility. *Atmos. Chem. Phys.* **2013**, *13*, 4895–4905. [[CrossRef](#)]
9. Sedlak, D.L.; Hoigné, J. The role of copper and oxalate in the redox cycling of iron in atmospheric waters. *Atmos. Environ. Part A Gen. Top.* **1993**, *27*, 2173–2185. [[CrossRef](#)]
10. Shi, Z.; Krom, M.D.; Jickells, T.D.; Bonneville, S.; Carslaw, K.S.; Mihalopoulos, N.; Baker, A.R.; Benning, L.G. Impacts on iron solubility in the mineral dust by processes in the source region and the atmosphere: A review. *Aeolian Res.* **2012**, *5*, 21–42. [[CrossRef](#)]
11. Vagnoni, F.; Illuminati, S.; Annibaldi, A.; Memmola, F.; Giglione, G.; Falgiani, A.M.; Girolametti, F.; Fanelli, M.; Scarponi, G.; Truzzi, C. Seasonal Evolution of the Chemical Composition of Atmospheric Aerosol in Terra Nova Bay (Antarctica). *Atmosphere* **2021**, *12*, 1030. [[CrossRef](#)]
12. Paris, R.; Desboeufs, K.; Journet, E. Variability of dust iron solubility in atmospheric waters: Investigation of the role of oxalate organic complexation. *Atmos. Environ.* **2011**, *45*, 6510–6517. [[CrossRef](#)]
13. Kieber, R.J.; Skrabal, S.A.; Smith, B.J.; Willey, J.D. Organic Complexation of Fe(II) and Its Impact on the Redox Cycling of Iron in Rain. *Environ. Sci. Technol.* **2005**, *39*, 1576–1583. [[CrossRef](#)] [[PubMed](#)]
14. Tapparo, A.; Di Marco, V.; Badocco, D.; D’Aronco, S.; Soldà, L.; Pastore, P.; Mahon, B.M.; Kalberer, M.; Giorio, C. Formation of metal-organic ligand complexes affects solubility of metals in airborne particles at an urban site in the Po valley. *Chemosphere* **2020**, *241*, 125025. [[CrossRef](#)] [[PubMed](#)]
15. Illuminati, S.; Annibaldi, A.; Bau, S.; Scarchilli, C.; Ciardini, V.; Grigioni, P.; Girolametti, F.; Vagnoni, F.; Scarponi, G.; Truzzi, C. Seasonal Evolution of Size-Segregated Particulate Mercury in the Atmospheric Aerosol Over Terra Nova Bay, Antarctica. *Molecules* **2020**, *25*, 3971. [[CrossRef](#)] [[PubMed](#)]
16. Casale, A.; Daniele, P.G.; de Robertis, A.; Sammartano, S. Ionic strength dependence of formation constants. Part XI. An analysis of literature data on carboxylate ligand complexes. *Ann. Di Chim. Chim.* **1988**, *78*, 249.
17. Sammartano, S.; Doria, A. Of Equilibrium Program for Computing Distribution Diagrams and Curves. *Comput. Chem.* **1989**, *13*, 343–359.
18. Goldberg, R.N.; Kishore, N.; Lennen, R.M. Thermodynamic Quantities for the Ionization Reactions of Buffers. *J. Phys. Chem. Ref. Data* **2002**, *31*, 231–370. [[CrossRef](#)]
19. Daniele, P.G.; De Robertis, A.; De Stefano, C.; Gianguzza, A.; Sammartano, S. Salt effects on the protonation of ortho-phosphate between 10 and 50°C in aqueous solution. A complex formation model. *J. Solut. Chem.* **1991**, *20*, 495–515. [[CrossRef](#)]

20. Daniele, P.G.; de Robertis, A.; De Stefano, C.; Sammartano, S.; Rigano, C. On the possibility of determining the thermo-dynamic parameters for the formation of weak complexes using a simple model for the dependence on ionic strength of activity coefficients: Na. *J. Chem. Soc. Dalt. Trans.* **1985**, *11*, 2353–2361. [[CrossRef](#)]
21. Academic Software. Sourby Old Farm, Timble, Otley, Yorks, LS21 2PW. In SC-Database. The IUPAC Stability Constant Database, Version 5.84.
22. De Robertis, A.; Rigano, C.; Sammartano, S.; Zerbinati, O. Ion association of Cl^- with Na^+ , K^+ , Mg^{2+} and Ca^{2+} in aqueous solution at $10 \leq T \leq 45$ °C and $0 \leq I \leq 1$ mol l^{-1} : A literature data analysis. *Thermochim. Acta* **1987**, *115*, 241–248. [[CrossRef](#)]
23. Millero, F.J.; Yao, W.; Aicher, J. The speciation of Fe(II) and Fe(III) in natural waters. *Mar. Chem.* **1995**, *50*, 21–39. [[CrossRef](#)]
24. Chughtai, A.R.; Marshall, R.; Nancollas, G.H. Complexes in calcium phosphate solutions. *J. Phys. Chem.* **1968**, *72*, 208–211. [[CrossRef](#)] [[PubMed](#)]
25. Smith, R.M.; Alberty, R.A. The Apparent Stability Constants of Ionic Complexes of Various Adenosine Phosphates with Divalent Cations. *J. Am. Chem. Soc.* **1956**, *78*, 2376–2380. [[CrossRef](#)]
26. Smith, R.M.; Martell, A.E. *Critical Stability Constants*; Plenum Press: New York, NY, USA, 1976.
27. Izatt, B.R.M.; Eatough, D.; Christensen, J.J.; Bartholomew, C.H. Calorimetrically Determined LogK, ΔH° , and ΔS° Values for the Inter- action of Sulphate Ion with Several Bi- and Ter-valent Metal Ions. *J. Chem. Soc. A* **1969**, *47*, 45–47. [[CrossRef](#)]
28. De Robertis, A.; Di Giacomo, P.; Foti, C. Ion-selective electrode measurements for the determination of formation constants of alkali and alkaline earth metals with low-molecular-weight ligands. *Anal. Chim. Acta* **1995**, *300*, 45–51. [[CrossRef](#)]
29. Horibe, Y.; Endo, K.; Tsubota, H. Calcium in the South Pacific, and its correlation with carbonate alkalinity. *Earth Planet. Sci. Lett.* **1974**, *23*, 136–140. [[CrossRef](#)]
30. Fabricand, B.P.; Imbimbo, E.S.; Brey, M.E.; Weston, J.A. Atomic absorption analyses for Li, Mg, K, Rb, and Sr in ocean waters. *J. Geophys. Res.* **1966**, *71*, 3917–3921. [[CrossRef](#)]
31. Culkin, F.; Cox, R.A. Sodium, potassium, magnesium, calcium and strontium in sea water. *Deep-Sea Res. Oceanogr. Abstr.* **1966**, *13*, 789–804. [[CrossRef](#)]
32. Legrand, M.; Preunkert, S.; Jourdain, B.; Aumont, B. Year-round records of gas and particulate formic and acetic acids in the boundary layer at Dumont d’Urville, coastal Antarctica. *J. Geophys. Res. Earth Surf.* **2004**, *109*. [[CrossRef](#)]
33. Legrand, M.; Gros, V.; Preunkert, S.; Sarda-Estève, R.; Thierry, A.-M.; Pépy, G.; Jourdain, B. A reassessment of the budget of formic and acetic acids in the boundary layer at Dumont d’Urville (coastal Antarctica): The role of penguin emissions on the budget of several oxygenated volatile organic compounds. *J. Geophys. Res. Earth Surf.* **2012**, *117*. [[CrossRef](#)]
34. Legrand, M.; Ducroz, F.; Wagenbach, D.; Mulvaney, R.; Hall, J. Role of polar ocean and penguin emissions. *J. Geophys. Res.* **1998**, *103*, 11043–11056. [[CrossRef](#)]
35. Litter, M.I.; Slodowicz, M. An overview on heterogeneous Fenton and photoFenton reactions using zerovalent iron materials. *J. Adv. Oxid. Technol.* **2017**, *20*. [[CrossRef](#)]